Atmos. Meas. Tech., 10, 1465–1479, 2017
www.atmos-meas-tech.net/10/1465/2017/
doi:10.5194/amt-10-1465-2017


Atmospheric Measurement Techniques
Open Access
EGU

# Development of a portable cavity-enhanced absorption spectrometer for the measurement of ambient $NO_3$ and $N_2O_5$: experimental setup, lab characterizations, and field applications in a polluted urban environment

**Haichao Wang**[1], **Jun Chen**[2], **and Keding Lu**[1]

[1]State Key Joint Laboratory of Environmental Simulation and Pollution Control, College of Environmental Sciences and Engineering, Peking University, Beijing, China
[2]College of Energy and Power Engineering, University of Shanghai for Science and Technology, Shanghai, China

*Correspondence to:* Keding Lu (k.lu@pku.edu.cn)

Received: 27 September 2016 – Discussion started: 10 October 2016
Revised: 26 March 2017 – Accepted: 28 March 2017 – Published: 19 April 2017

**Abstract.** A small and portable incoherent broadband cavity-enhanced absorption spectrometer (IBBCEAS) for $NO_3$ and $N_2O_5$ measurement has been developed. The instrument features a mechanically aligned non-adjustable optical mounting system, and the novel design of the optical mounting system enables a fast setup and stable operation in field applications. To remove the influence of the strong nonlinear absorption by water vapour, a dynamic reference spectrum through NO titration is used for the spectrum analysis. The wall loss effects of the sample system were extensively studied, and the total transmission efficiencies were determined to be 85 and 55 % for $N_2O_5$ and $NO_3$, respectively, for our experimental setup. The limit of detection (LOD) was estimated to be 2.4 pptv ($1\sigma$) and 2.7 pptv ($1\sigma$) at 1 s intervals for $NO_3$ and $N_2O_5$, respectively. The associated uncertainty of the field measurement was estimated to be 19 % for $NO_3$ and 22–36 % for $N_2O_5$ measurements from the uncertainties of transmission efficiency, absorption cross section, effective cavity length, and mirror reflectivity. The instrument was successfully deployed in two comprehensive field campaigns conducted in the winter and summer of 2016 in Beijing. Up to 1.0 ppb $NO_3$+$N_2O_5$ was observed with the presence of high aerosol loadings, which indicates an active night-time chemistry in Beijing.

## 1 Introduction

The nitrate radical ($NO_3$) and dinitrogen pentoxide ($N_2O_5$) are the most important reactive nitrogen species in night-time chemistry (Wayne et al., 1991). The $NO_3$ is dominantly formed by the reaction of $NO_2$ with $O_3$ (Reaction R1), which contributes to the night-time oxidation of volatile organic compounds (VOCs; Reaction R2) and the production of the organic nitrate (Fry et al., 2009; Riemer et al., 2003). $NO_3$ can react with NO rapidly (Reaction R3), and $NO_3$ absorbs red light effectively by its strong $B^2E'$-$X^2A_2'$ electronic transition centred around 662 nm (Yokelson et al., 1994). Such strong absorption in the visible light range promotes the development of optical instruments applied in ambient $NO_3$ detection. After formation, $NO_3$ holds a thermal exchange with $N_2O_5$ (reactions R4a and b), which is defined by the $NO_2$ concentration and the ambient temperature (Brown et al., 2003a). The heterogeneous reaction of $N_2O_5$ on ambient aerosols plays an important role on the $NO_x$ removal from regional to global scales (Brown et al., 2006; Brown and Stutz, 2012; H. C. Wang et al., 2015) and shows a potentially significant impact on the ambient $RO_x$ chemistry and photochemical ozone productions through halogen activation (Reaction R5; Osthoff et al., 2008; Thornton et al., 2010; Phillips et al., 2012; Tham et al., 2016).

$$NO_2 + O_3 \rightarrow NO_3, \quad \text{(R1)}$$

$$NO_3 + \text{VOCs} \rightarrow \text{products}, \quad \text{(R2)}$$

$$NO_3 + NO \rightarrow 2NO_2, \quad \text{(R3)}$$

$$NO_2 + NO_3 + M \rightarrow N_2O_5 + M, \quad \text{(R4a)}$$

$$N_2O_5 + M \rightarrow NO_2 + NO_3 + M, \quad \text{(R4b)}$$

$$N_2O_5 + (H_2O \text{ or } Cl^-) \rightarrow (2-\phi)NO_3^- + \phi ClNO_2. \quad \text{(R5)}$$

$NO_3$ is a radical with a short lifetime, high reactivity, and an extremely low mixing ratio in ambient air (Wayne et al., 1991), which means that field-deployable $NO_3$ measurement techniques should feature high sensitivity, high selectivity, and high temporal and spatial resolutions. The requests are less rigorous for detection of $N_2O_5$, since, in general, it has higher concentrations and less reactivity than $NO_3$.

There are several existing methods based on optical spectroscopy and mass spectrometry for the in situ detection of $NO_3$ and $N_2O_5$. With respect to the optical approaches, $NO_3$ detection is based on its strong absorption around 662 nm (Yokelson et al., 1994), and $N_2O_5$ can be measured following thermal dissociation to $NO_3$. Since the 2000s, cavity ring-down spectroscopy (CRDS) has been used in the field measurement of both $NO_3$ and $N_2O_5$ (Simpson, 2003; Brown et al., 2002; Dubé et al., 2006; Nakayama et al., 2008; Schuster et al., 2009). CRDS has high temporal and spatial resolution with high sensitivity and accuracy. Cavity-enhanced absorption spectroscopy (CEAS) was proposed later by Fiedler et al. (2003) and has been successfully deployed to measure a number of atmospheric trace gas compounds like HONO, $H_2O$, IO, $O_3$, $O_4$, $I_2$, IO, OIO, $SO_2$, $NO_3$, $N_2O_5$, glyoxal (CHOCHO), and methylgloxal ($CH_3COCHO$; Washenfelder et al., 2008, 2013, 2016; Thalman and Volkamer, 2010; Gherman et al., 2008; Axson et al., 2011; Kahan et al., 2012; Min et al., 2016). The measurement of $NO_3$ was shown to be successful in simulation chamber conditions with an open-path incoherent broadband CEAS setup (Venables et al., 2006; Varma et al., 2009), and shortly afterwards, the closed cavity type of IBBCEAS was successfully deployed on the ground (Langridge et al., 2008; Benton et al., 2010) and airborne (Kennedy et al., 2011) for measurements of both $NO_3$ and $N_2O_5$. According to comparison experiments at the SAPHIR chamber (Fuchs et al., 2012; Dorn et al., 2013), the CEAS technique shows a similar detection capability for $N_2O_5$ and $NO_3$ to that of CRDS (e.g. Brown et al., 2003b, 2006; Benton et al., 2010; Kennedy et al., 2011; Crowley et al., 2010; Sobanski et al., 2016). For the laser-induced fluorescence (LIF), its detection sensitivity is, in general, smaller than that of the cavity-assisted absorption techniques due to the low fluorescence quantum yield of $NO_3$ (Matsumoto et al., 2005). In addition to optical approaches, different chemical ionization mass spectrometry (CIMS) methods have been used for the detection of ambient $N_2O_5$ (Slusher et al., 2004; Fortner et al., 2004; Kercher et al., 2009; Chang et al., 2011). Slusher et al. (2004) utilized ion reaction ($I^- + N_2O_5 \rightarrow NO_3^-$) to detect $N_2O_5$ at 62 amu ($NO_3^-$). Nevertheless, this approach showed cross sensitivity towards $NO_3$ ($I^- + NO_3 \rightarrow NO_3^-$) and additional interference from species like $ClONO_2$ and $BrONO_2$. A strong unknown interference at 62 amu was found for the detection of $N_2O_5$ under a high-$NO_x$ regime in Hong Kong (Wang et al., 2014). Kercher et al. (2009) introduced an ion-molecule region (IMR) module wherein the ion reaction, $I^- + N_2O_5 \rightarrow I(N_2O_5)^-$, is enhanced so that $N_2O_5$ can be detected specifically at 235 amu. With this method, a direct measurement of $N_2O_5$ is achieved, showing a good comparison with the well-established CRDS system in Hong Kong (Wang et al., 2016).

Until now, field measurements of $NO_3$ and $N_2O_5$ have been extensively conducted in both the United States of America (USA) and Europe but have been sparse in China (i.e. Brown et al., 2006; Crowley et al., 2010; Benton et al., 2010), with only a few conducted in Hong Kong, Shanghai, and the North China Plain (Wang et al., 2016, 2013; Brown et al., 2016; Tham et al., 2016). From satellite observations, it was found that the USA, Europe, and China are the three major high-$NO_x$ regions worldwide (e.g. Richter et al., 2005). Moreover, in the North China Plain areas, the high-$NO_x$ air masses often overlap with high aerosol loadings from both secondary aerosol particle formation as well as nearby natural sources (e.g. dust from the Gobi Desert in the spring) and serve as ideal locations for the study of $NO_3$ and $N_2O_5$ chemistry. To probe such potentially interesting chemistry in China, we developed a new light-emitting diode (LED)-based IBBCEAS (incoherent broadband cavity-enhanced absorption spectrometer) instrument for the detection of $NO_3$ and $N_2O_5$. In this study, the detailed setup of our instrument, lab characterizations, and its first field applications in Beijing are presented.

## 2 The instrument

Our IBBCEAS instrument is designed to measure the ambient $NO_3$ and $N_2O_5$ and features a small size, easy portability, and low power consumption. The total weight is less than 25 kg, approximate dimensions are $95 \times 40 \times 25$ cm, and the power consumption is less than 300 W, which potentially meets the requirements for future applications on mobile platforms. The system is distinct from previous IBBCEAS systems (Langridge et al., 2008; Schuster et al., 2009; Kennedy et al., 2011) because of its rigid cavity design, fast setup, and stable operation (e.g. the thermal alignment drift is minimized) in field campaigns. A dynamic NO titration setup was used to obtain the reference spectrum, which removed the influence of ambient water vapour so that the fitting precision was significantly enhanced.

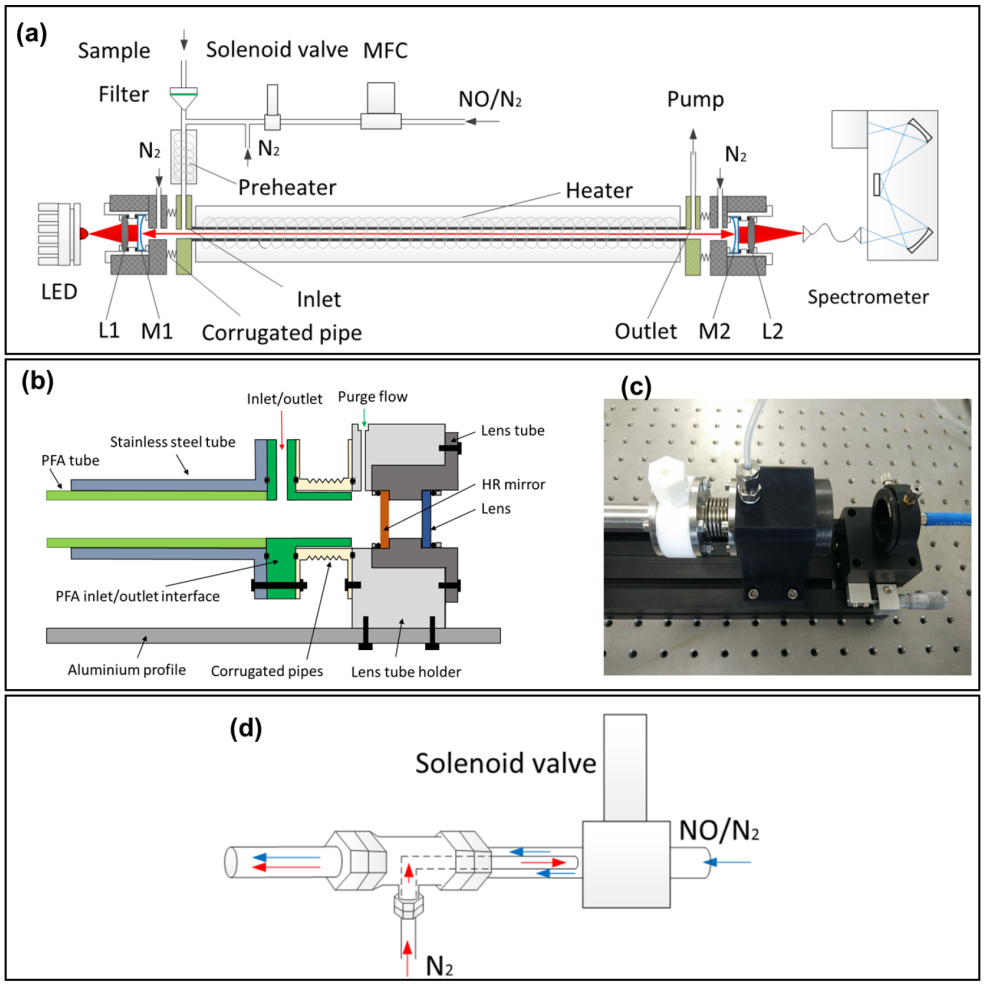


**Figure 1.** A schematic of the newly developed IBBCEAS instrument for the detection of $NO_3$ and $N_2O_5$. **(a)** Overview of the optical layout (LEDs, collimating optics, high-finesse cavity, and spectrometer) and the flow system (aerosol filter, inlet, NO titration module, preheating tube, and detection cell). **(b)** The schematic layout of the mirror mounts, which enables a mechanical alignment of the high-reflectivity (HR) mirrors. **(c)** A photograph of the mirror mounts. **(d)** The schematic layout of the NO titration module; the red arrow denotes the $N_2$ gas flow, and the blue arrow denotes the NO gas flow.

### 2.1 Optical layout

The schematic layout of the instrument is shown in Fig. 1a. The optical layout consists of a temperature stabilized light source, collimating optics, and a commercial spectrograph with a charge-coupled device (CCD) detector. The light source and collimating optics were concentrically integrated on an aluminium profile ($75 \times 8 \times 5$ cm).

A single-colour LED (LZ1-10R200, LED Engin, Marblehead, MA, USA) is used as the light source and is mounted on a three-dimensional (3-D) adjustable bracket. The manufacturer-specified full luminosity output is about 800 mW, centred at the deep red light region (660 nm), and the full width at half maximum (FWHM) is 25 nm. To minimize the wavelength shift and intensity drift caused by the LED temperature drift, the LED plate is mounted on an aluminium block and uses a thermoelectric cooler control module to stabilize the temperature of the aluminium block at $17.5 \pm 0.1$ °C. The aluminium block is thermally insulated to reduce heat exchange with the ambient surroundings.

Before light is emitted into the high-finesse cavity, a plano-convex lens ($f = 30$ mm) is concentrically installed into the lens tube (shown in Fig. 1a as L1) to collimate the red light into the high-finesse cavity. The high-finesse cavity is formed by a pair of high-reflectivity (HR) mirrors (102116, Layertec GmbH, Mellingen, Germany) with a diameter of 25.0 mm ($+0.00/-0.10$ mm). The peak reflectivity of the HR mirrors at 660 nm is reported to be larger than 99.99 % with a radius curvature of $100 \pm 5$ cm. The two HR mirrors are mounted on two customized lens tubes, and the lens tubes are mechanically mounted on two matching lens tube holders, which are installed on an aluminium profile to maintain the dis-

tance between the two mirrors at 50.0 cm. Due to the high-precision machining and assembly, the two lens tubes (shown as the scheme in Fig. 1b and the corresponding photograph in Fig. 1c) and the HR mirrors are mechanically aligned to have concentricity ($< 0.01°$). Each HR mirror is continuously purged by 100 mL min$^{-1}$ high-purity nitrogen flow to prevent particle contamination by the sample gas flow.

The optical cavity is enclosed by a sample gas detection cell with a sample inlet, outlet, and two welded corrugated pipes connected at two ends. The light exiting the cavity is further imaged by a plano-convex lens ($f = 50$ mm) installed on the lens tube (shown in Fig. 1a as L2) that couples the output light onto the lead of a 100 µm diameter, 0.22 numerical aperture optical fibre (QP100-2-UV-VIS, Ocean Optics, Dunedin, FL, USA). The lead of the fibre is mounted on a 3-D adjustable bracket and integrated on the aluminium profile. The other lead of the fibre directs the cavity output light into the spectrometer (QE65PRO, Ocean Optics, Dunedin, FL, USA). The CCD in the QE65000 spectrograph is thermally regulated at $-20.0$ °C to minimize the dark current. The line density of the diffraction grating of the spectrometer is 1200 mm$^{-1}$, the entrance slit width is 100 µm, and the spectral resolution FWHM is 0.85 nm with the wavelength coverage of 580–710 nm. The instrument works under a signal-to-noise ratio estimated to be larger than 500 : 1.

### 2.2 Flow system

The instrument sample flow system includes the aerosol filter, the inlet tube, the preheating tube and heated detection cell, and sensors for temperature, pressure, and relative humidity. During the field measurements, we operate with a sample flow rate of 2.0 L min$^{-1}$. A Teflon polytetrafluoroethylene (PTFE) filter (25 µm thickness, 4.6 cm diameter, 2.5 µm pore size, Typris, China) is used in the front of the sample module to remove ambient aerosols. After the filtration of the aerosols, the sample gas flow is delivered into the preheating tube through a 1.5 m perfluoroalkoxy alkanes (PFA) inlet tube (Entegris, I.D. = 4.35 mm). A 35 cm long PFA tube (Entegris, I.D. = 4.35 mm) is installed in the front of the inlet interface as a preheating tube to dissociate $N_2O_5$ to $NO_3$. This preheating tube is heated and stabilized at 120 °C. With this setup of temperature and residence time, $N_2O_5$ is completely decomposed to $NO_3$ in the preheating tube.

In Fig. 1b, the central part of the detection cell is constructed using a 35.6 cm long PFA tube (marked in light green; Entegris, I.D. = 10.0 mm), enclosed by a stainless steel tube (marked in grey). Each end of the stainless steel tube is connected with a PFA interface (marked in green) which set up the inlet and outlet and further connected with the corrugated pipes. With this combination, the loss of $NO_3$ during detection is minimized. The total PFA cell length is 44.0 cm, but the length from the inlet to the outlet is only 39.2 cm. The sample gas flow cell is heated and stabilized at 80 °C to prohibit the reverse reaction of $NO_3$ and $NO_2$ producing $N_2O_5$.

### 2.3 Dynamic reference spectrum

The effect of non-Beer–Lambert behaviour of water vapour absorption lines near 660 nm has to be well accounted for to achieve accurate and precise $NO_3$ detection (Langridge et al., 2008; Dorn et al., 2013). A few groups reported that the water vapour absorption can be determined with an "effective" water vapour absorption cross section from a look-up table approach or a real-time iterative calculation approach under atmospheric conditions (Varma et al., 2009; Langridge et al., 2008; Kennedy et al., 2011). In this work, we solve this problem by using a dynamic reference spectrum through frequent addition of NO into the inlet. This method has previously been used to acquire the chemical zero in the CRDS method (Brown et al., 2002; Crowley et al., 2010). Through the frequent addition of NO, the reference spectrum contain optical extinction from other absorbers in this spectral region, for example water vapour, $NO_2$, $O_3$, and any aerosols not removed by the filter. For the CRDS method, the NO addition is carefully designed so that the resulting extinction of increased $NO_2$ in the reference measurement compared to that of $NO_3$ is negligible. For the CEAS method, the NO addition is a little less precise since this method allows for observation of $NO_3$ separately from $NO_2$ due to their different spectral shapes. In both cases, the effect of water vapour is removed, and the fitting precision increases significantly in our applications.

The NO titration module is connected to the inlet tube by a PFA tee-piece. Using a computer-controlled solenoid valve, the instrument measures reference and sample spectrum sequentially by switching the NO injection on and off (NO = 98.0 ppmv, flow rate = 10.0 mL min$^{-1}$). A high-purity $N_2$ line (I.D. = 1.50 mm) is added at the exit of the solenoid valve by a PFA tee-piece to flush the residual NO after the NO injection is switched off (Fig. 1d). The resulting NO mixing ratio is about 480 ppbv in the sample flow when NO injection is performed. Since 8.0 ppbv $N_2O_5$ was once observed and reported in Hong Kong (Wang et al., 2016) as an extreme case, the ambient $NO_3$, $N_2O_5$, and $O_3$ were set at about 1, 10, and 100 ppbv, respectively, for the simulation, proving that the ambient $NO_3$ and $N_2O_5$ can be removed within a time scale of 0.05 s when NO is injected (Fig. 2).

The $NO_2$ impurity in the used NO standard is analysed by a commercial $NO_x$ instrument (TE-42i). The $NO_2$ impurity is found to be around 0.8 %, which means 4 ppbv of $NO_2$ is present in the reference spectrum measurement with the presence of 480 ppbv NO. The $NO_3$ and $O_3$ in the preheating tube and detection cell react with the high concentration of NO and generate $NO_2$. In the case shown as Fig. 2, the additional $NO_2$ produced during the measurement of the reference spectrum can reach up to 55 ppbv (with the initial additional $NO_2$ set at 4 ppbv). Therefore, to use this dynamic ref-

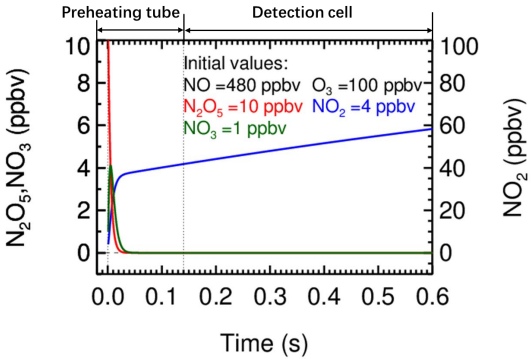


**Figure 2.** Simulation of the change of the mixing ratios of $NO_3$, $N_2O_5$, and $NO_2$ during the NO titration mode in the preheating tube and detection cell for an extremely high $NO_3$ and $N_2O_5$ case. The initial ambient $NO_3$, $N_2O_5$, and $O_3$ were set at 1, 10, and 100 ppbv, respectively. The initial $NO_2$ was set at 4 ppbv from the impurity of the used NO standard.

erence spectrum, we normally fit both $NO_3$ and $NO_2$ to cover the limiting cases when the generated $NO_2$ is high. Nevertheless, the fitted $NO_2$ concentration will be negative since the $NO_2$ concentrations are higher in the reference spectrum.

## 3 Characterizations

The principle of the IBBCEAS system was systematically introduced by Fiedler et al. (2003) and will only be introduced briefly here. The extinction coefficient ($\alpha(\lambda)$) in the cavity intrinsically consists of the absorption, the Rayleigh, and the Mie scattering, caused by the gas samples (Eq. 1). The $\alpha(\lambda)$ can be determined through measurements of the intensity of the sample spectrum, the reference spectrum, the mirror reflectivity, and the effective cavity length

$$\alpha(\lambda) = \left(\frac{I_0(\lambda)}{I(\lambda)} - 1\right)\left(\frac{1 - R(\lambda)}{d_{\text{eff}}}\right) = \sum_i n_i \times \sigma_i(\lambda) + \alpha_{\text{Mie}}(\lambda) + \alpha_{\text{Rayl}}(\lambda). \quad (1)$$

In Eq. (1), $\lambda$ is the wavelength of light; $n_i$ and $\sigma_i(\lambda)$ are the number density and absorption cross section of the $i$th gas compound, respectively, which causes absorption of the incident light; $d_{\text{eff}}$ is the effective cavity length; $R(\lambda)$ is the mirror reflectivity; $\alpha_{\text{Rayl}}(\lambda)$ is the extinction due to Rayleigh scattering; $\alpha_{\text{Mie}}(\lambda)$ is the extinction due to Mie scattering; $I_0(\lambda)$ is the reference spectrum; and $I(\lambda)$ is the sample spectrum. According to Eq. (1), the parameters include the cross section of the strong light absorbing gases in the target wavelength range, the effective cavity length, and the mirror reflectivity that has to be quantified.

### 3.1 The absorption cross section ($\sigma_i(\lambda)$)

The effective absorption cross section of the abundant ambient absorbers, $NO_3$ and $NO_2$, in the wavelength window of 640–680 nm needs to be determined to retrieve the molecule number density of $NO_3$. Since we used a dynamic reference spectrum, which contains the same amount of water vapour as that of the measured sample spectrum (Sect. 2.3), the calculation of the strong nonlinear absorption lines of $H_2O$ in this wavelength window is avoided. The $NO_3$ absorption cross section is known to be temperature dependent (Wangberg et al., 1997; Sander, 1986; Ravishankara and Mauldin, 1986; Yokelson et al., 1994; Orphal et al., 2003; Osthoff et al., 2007). Under the heated cavity conditions (353 K), the effective absorption cross section of $NO_3$ is calculated by two steps: (1) the reported cross section of $NO_3$ (Yokelson et al., 1994) is scaled to the ratio of the band's peak intensity at 662 nm between 298 and 353 K according to Osthoff et al. (2007) and (2) the scaled absorption cross section is further convoluted with an instrument function determined with the neon emission line at 659.48 nm. Consequently, the calculated effective cross section at 353K is about $1.77 \times 10^{-17}$ cm$^2$ molecule$^{-1}$ at 662 nm, and the uncertainty of the temperature correction and convolution is estimated to be 13 %. Under cold cavity conditions (298 K), the $NO_3$ cross section is convoluted directly to our spectral resolution with a peak value of $2.02 \times 10^{-17}$ cm$^2$ molecule$^{-1}$ at 662 nm, and the uncertainty of the convolution is estimated to be 10 % (Kennedy et al., 2011). The $NO_2$ cross section is reported to be not sensitive to the temperature change (Voigt et al., 2002), so that only convolution is performed to derive its effective absorption cross section for our instrument setup. Figure 3 shows the temperature-scaled and instrumental resolution convolved $NO_3$ absorption cross section at 353 K and the convolved $NO_2$ absorption cross section, respectively. The cross section of $NO_3$ near 662 nm is three orders of magnitude larger than that of $NO_2$.

### 3.2 The mirror reflectivity ($R(\lambda)$)

The mirror reflectivity ($R(\lambda)$) is an important parameter to be determined for the CEAS type of instrument. In previous work, $R(\lambda)$ had been determined through four different methods, including the detection of a stable trace gas compound with known concentrations (Venables et al., 2006), the differentiation of pure gases with distinct Rayleigh scattering cross sections (Chen and Venables, 2011; Washenfelder et al., 2016; Min et al., 2016), the usage of low-loss optics (Varma et al., 2009), and the determination of the phase shift or ring down time (Langridge et al., 2008; Schuster et al., 2009; Kennedy et al., 2011). In this study, $R(\lambda)$ is determined through the differentiation of pure gases ($N_2$ and He) in the cavity (Eq. 2) during the field campaigns. The Rayleigh scattering cross sections for $N_2$ ($\sigma_{\text{Rayl,N}_2}(\lambda)$) and He ($\sigma_{\text{Rayl,He}}(\lambda)$) are found in Sneep and Ubachs (2005) and

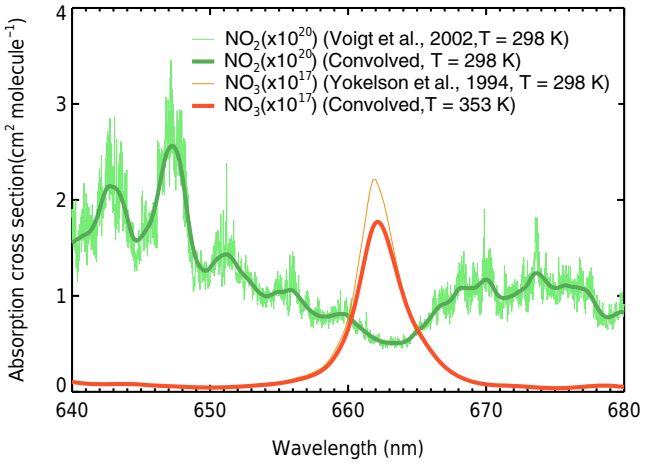


**Figure 3.** Absorption cross section of $NO_3$ and $NO_2$ from 640 to 680 nm. The green thin line is the original cross section of $NO_2$ at 298 K determined by Voigt et al. (2002), the green thick line is the convolved result, the orange thin line is the original cross section of $NO_3$ at 298 K determined by Yokelson et al. (1994), and the red thick line is the temperature-scaled and convolved cross section at 353 K.

Shardanand and Rao (1977), respectively.

$$R(\lambda) = 1 - d \times \left( \frac{I_{N_2}(\lambda) \times n_{N_2} \times \sigma_{Rayl,N_2}(\lambda) - I_{He}(\lambda) \times n_{He} \times \sigma_{Rayl,He}(\lambda)}{I_{He}(\lambda) - I_{N_2}(\lambda)} \right). \quad (2)$$

In Eq. (2), $d$ is the distance between the two high-reflectivity mirrors (50.0 cm); $I_{N_2}(\lambda)$ and $I_{He}(\lambda)$ represent the light out spectrum determined when the cavity is filled by $N_2$ or He through the purge flow injection lines, respectively; and $n_{N_2}$ and $n_{He}$ are the calculated number density of $N_2$ and He, respectively, at the measured temperature and pressure in the cavity. Figure 4 shows the mirror reflectivity calibration results during the field measurements performed at the campus of the University of Chinese Academy of Science (UCAS) in Beijing during winter 2016. The bold black line is the average reflectivity of the five measurements of $R(\lambda)$. It is noted that the peak of $R(\lambda)$ is $0.999936 \pm 0.000002$ at 662 nm. Under the protection of the purge flow and due to the mechanically aligned setup of the cavity system, the determined $R(\lambda)$ is remarkably stable during this field campaign. The bold red line is the average cavity loss, which is equal to $(1 - R(\lambda))/d$, with the maximized point near 662 nm of $(1.28 \pm 0.01) \times 10^{-6}$ ($1\sigma$). The total uncertainty of the reflectivity is about 5 %, which is dominated by the scattering cross sections of $N_2$, according to Sneep and Ubachs (2005). The uncertainty for He makes a negligible contribution (Washenfelder et al., 2008).

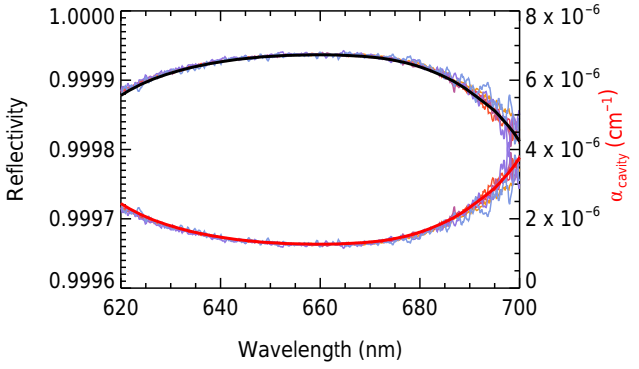


**Figure 4.** Mirror reflectivity and cavity losses calibrated with high-purity He and $N_2$ in the current experimental setup during the field measurements. The original calibration results were depicted by varying coloured lines: the smoothed black bold line is the average $R(\lambda)$, and the smoothed bold red line is the average cavity loss $((1 - R(\lambda))/d)$ from five measurements. The mean ($\pm 1\sigma$) value at 662 nm of reflectivity and the cavity loss are $0.999936 \pm 0.000002$ and $(1.28 \pm 0.01) \times 10^{-6}$, respectively. The effective path length at 662 nm reached 6.13 km.

### 3.3 The effective cavity length ($d_{eff}$)

The effective cavity length ($d_{eff}$) represents the cavity length occupied by the absorbing gas when the sample flow is stable. Since the continuous purge flow occupies the two ends of the cavity to protect the mirrors, the $d_{eff}$ is usually shorter than the distance between the two high-reflectivity mirrors (defined as $d$, which is 50.0 cm in our setup) and longer than the distance between the sample inlet and outlet (defined as $d_{sample}$, which is 39.2 cm in our setup). We determine the $d_{eff}$ by supplying an $NO_2$ gas standard (200 ppbv) with a constant flow into the cavity with purge flow and by retrieving the $d_{eff}$ based on Eq. (1). The 200 ppbv $NO_2$ sample is prepared by a bottle standard of $NO_2$ (80.8 ppm) diluted with high-purity synthetic air ($O_2$: 20.5 %, $N_2$: bal) through a gas mixer (TE-146i). The uncertainty of the prepared $NO_2$ standard is estimated to be 2 %, while the uncertainty of the $NO_2$ absorption cross section is estimated to be 4.7 % according to Voigt et al. (2002). In our measurement, the $d_{eff}$ is determined to be 45.0 cm, which occupies 90.0 % of the total length of the optical cavity. Moreover, $d_{sample}$ is 78.4 % of the length of the total optical cavity. The $d_{sample}$ is shorter than $d_{eff}$, indicating that there is turbulent mixing of sample gas into the purge volumes. Since the possibility of this turbulent mixing is slow relative to the rate of the $NO_3$ wall losses, the determination of the $d_{eff}$ for $NO_3$ is associated with an additional uncertainty of 12 %, and the total uncertainty of the determined $d_{eff}$ with this approach is about 13 %.

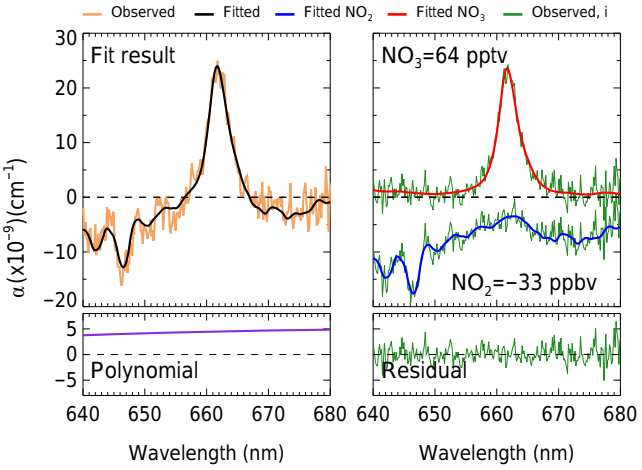


**Figure 5.** An example of the spectral fit for an extinction spectrum measured (5 s average) during field measurements. The fitted results of $NO_3$ and $NO_2$ are shown as well as the third-order polynomial, the total fit result, and the residual.

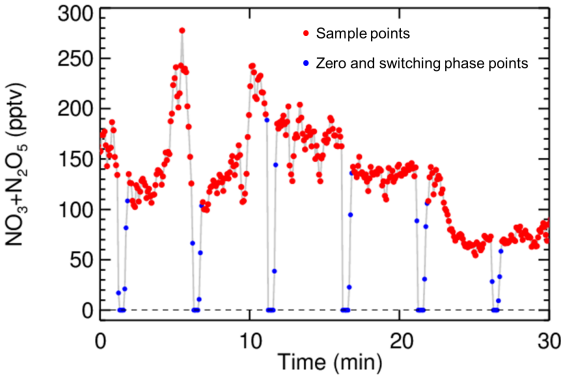


**Figure 6.** An example time series of $NO_3 + N_2O_5$ detection performed at a rural site in Beijing with 5 s spectrum integral time. The red points denote the ambient measurement mode without NO addition, and the blue points denote the 20 s zero points (determination of the dynamic reference spectrum) with NO addition and 20 s switching time between the titration mode and the sample mode.

## 4 Results and discussion

### 4.1 Spectral fitting

A least-squares spectral fitting software package was developed for retrieving the molecule number densities of $NO_3$ and $NO_2$. The optimized spectral fitting window was found to be from 640 to 680 nm, and a third-order polynomial was applied to fit the background drift and unaccounted scattering effect. Figure 5 shows an example of the spectral fitting of a measurement spectrum of $NO_3$ at 5 s integration time with ambient measurement. By using the dynamic reference spectrum, the spectral fitting is targeted at $NO_3$ and $NO_2$ as explained above. The retrieved mixing ratio of $NO_3$ (that actually represents the $NO_3 + N_2O_5$ concentration in the gas samples) is 64 pptv and that of $NO_2$ is −33 ppbv, which was mainly caused by the conversion of ambient $O_3$ (80 ppbv) with the added NO in the measurement of the reference spectrum. The corresponding fitting residual is in the range of $\pm 4.0 \times 10^{-9}$ cm$^{-1}$, and the $H_2O$ absorption is found to be cancelled out in the residual spectrum. Moreover, an example time series of $NO_3 + N_2O_5$ measurement results during ambient measurements is shown in Fig. 6. During ambient measurement, the NO titration is performed periodically to acquire the dynamic reference spectrum. In Fig. 6, the red points mark the effective ambient measurement result, which covered 4 min 20 s of every 5 min, and the blue points include 20 s for the zero points and a 20 s switching phase between the two modes, which is discarded from the data analysis.

### 4.2 Transmission efficiency of $NO_3$ and $N_2O_5$

For the accurate measurement of $NO_3$ and $N_2O_5$, the wall loss reactivity of the sample manifold and the detection cell need to be determined. This includes (1) the wall loss on the filter, (2) the wall loss on the inner surface of the inlet tube, and (3) the wall loss in the preheating tube and the detection cell. To determine the wall loss reactivity, an $NO_3/N_2O_5$ source module with stable mixing ratio (±2 %) is set up in the lab. In this module, high-purity synthetic air and $NO_2$ is supplied to a gas mixer (TE-146i), and $O_3$ is generated in this gas mixer through the irradiation of a mercury lamp. The supplied $NO_2$ and the produced $O_3$ is further delivered into a 160 L smog chamber to generate stable concentrations of $NO_3$ and $N_2O_5$. Commercial $NO_x$ (TE-42i) and $O_3$ monitors (TE-49i) are operated to quantify the mixing ratio of $NO_2$ and $O_3$ in the chamber. According to the detected concentration of $NO_2$ and $O_3$, we can modulate the delivered concentration levels of $NO_3$ and $N_2O_5$ with the help of a box model.

#### 4.2.1 Filter loss

The filter transmission efficiency of $NO_3$ and $N_2O_5$ is determined through the differentiation of an inlet without a filter, with a clean filter (25 µm thickness, 4.6 cm diameter, 2.5 µm pore size, Typris, China), and with used filters saved during typical pollution episodes during field measurements. According to previous field measurements of $NO_3$ and $N_2O_5$ (e.g. Brown et al., 2001; Schuster et al., 2009), frequent filter change is suggested, and the frequency is proposed to be 0.5–3 h, depending on the aerosol loadings to reduce the impact of the filter aging caused by aerosol accumulation. For this reason, we changed the filter with a regular time interval (once every hour) during pollution episodes. For clean conditions, the filter exchange frequency was reduced to be once every 2 h.

For the determination of the $NO_3$ filter transmission efficiency, an additional preheating tube is inserted in front of the

detection system to convert all the generated $N_2O_5$ delivered by the calibration source to $NO_3$. The determined clean filter transmission efficiency is 75 % for $NO_3$ and is slightly lower than the previous results of $NO_3$ transmission efficiency on Teflon filters (Aldener et al., 2006; Schuster et al., 2009). The filter transmission efficiency of $NO_3$ on used filters is determined to be 5 % less than on the clean filter. For the field calculation of the $NO_3$ concentrations, the filter transmission efficiency is then estimated to be $72 \pm 3$ %. For the determination of the $N_2O_5$ filter transmission efficiency, the mixing ratio of $NO_2$ and $O_3$ is modulated to achieve a high ratio of $N_2O_5/NO_3$ (> 100) before being fed into the instrument. The transmission efficiency of the $N_2O_5$ on the clean filter is determined to be 96 %, which is consistent with the previous studies on the filter loss of $N_2O_5$ (Fuchs et al., 2008; Aldener et al., 2006; Schuster et al., 2009). The filter transmission efficiency of $N_2O_5$ on a used filter is determined to be 6 % smaller than on the clean filter. Therefore, the filter transmission factor for $N_2O_5$ is estimated to be $93 \pm 3$ %.

#### 4.2.2 Wall loss of the inlet tube, the preheating tube, and the detection cell

To determine the wall loss reactivity of $NO_3$, the heated detection cell is used as a flow tube. Gas samples with a stable amount of $N_2O_5$ are delivered by the $NO_3/N_2O_5$ source described above. By stopping the sample gas flow, the observed $NO_3$ versus the elapsed time determines the first-order loss rate of $NO_3$ in the heated detection cell. In this experiment, the fitted first-order uptake coefficient of $NO_3$ reflects the contribution from three processes: (1) the wall loss of $NO_3$ in the detection cell, (2) the change of the effective cavity length due to the adding of the purge flows, and (3) the production of $NO_3$ from the reaction of $NO_2$ and $O_3$. The $NO_2$ concentration determined in the running sample gas flow is used to determine the change of $d_{\mathrm{eff}}$ corresponding to the elapsed time after stopping the sample flow (in the way it is used to quantify the $d_{\mathrm{eff}}$ in Sect. 3.3). A time series of $d_{\mathrm{eff}}$ is determined with high time resolution data acquisition (0.5 s) that is then used to quantify the mixing ratio of $NO_3$ in the corresponding time intervals. Figure 7 shows the decay of the observed $NO_3$ concentrations on a logarithmic scale versus the elapsed time. The fitted first-order decay rate is $0.13 \pm 0.02\,\mathrm{s}^{-1}$, with a good correlation coefficient ($R^2 = 0.991$). Finally, the fitted first-order decay rate is corrected by the chemistry of reactions R1 and R4 with a box model constrained to observed $NO_2$ and $O_3$. The $NO_3$ wall reactivity of the heated detection cell surface is determined to $0.16 \pm 0.02\,\mathrm{s}^{-1}$, which is similar to previous results of 0.1–0.3 $\mathrm{s}^{-1}$ (Brown et al., 2002; Crowley et al., 2010; Kennedy et al., 2011; H. C. Wang et al., 2015).

The surface materials are the same as that of the inlet tube, the preheating tube, and the detection cell. Therefore, the wall loss reactivity of $NO_3$ in the detection cell will be applicable for the inlet and the preheating tubes. As shown in Fig. 1a, our instrument has only one mixing point at the setup of the NO titration module. In addition, there is no blockage of the main sample gas flow of the PFA tee-piece. Therefore, we think the influence of the mixing point can be neglected. As reported by Kennedy et al. (2011), the $NO_3$ wall loss reactivity in the cold PFA piping (inlet) is the same as in the heated ones with a value of $0.27\,\mathrm{s}^{-1}$. Nevertheless, we noticed that Crowley et al. (2010) reported that the $NO_3$ wall loss reactivity of the cold PFA tube could be a factor of 2 larger than that of the heated tube. We assume our $NO_3$ wall loss reactivity for the cold PFA tube to be between 0.16 and $0.32\,\mathrm{s}^{-1}$, and the average $NO_3$ wall loss reactivity for the cold PFA tube is estimated to be $0.24\,\mathrm{s}^{-1}$ with an uncertainty of $0.08\,\mathrm{s}^{-1}$.

To determine the wall loss reactivity of the $N_2O_5$ in the PFA inlet tube, PFA tubes (Entegris, I.D. = 4.35 mm) with different lengths (0.5, 3.5, 5.5, 7.5, and 10.5 m) are inserted between the outlet of the $NO_3/N_2O_5$ source and the inlet of the preheating tube. The apparent first-order loss rate of $N_2O_5$ ($0.015\,\mathrm{s}^{-1}$) is deduced by an exponential fit of the observed $N_2O_5$ concentrations to the varied residence times with different tube lengths (Fig. 8). The actual situation is more complicated in these PFA tubes due to the reaction of R1, R4a and b, and the wall losses of both $NO_3$ and $N_2O_5$. The wall loss reactivity of $N_2O_5$ is retrieved from the observed apparent decay rate with a box model. In this model, initial $NO_2$ and $O_3$ are the observed values of the $NO_3/N_2O_5$ source. The retrieved $N_2O_5$ wall loss reactivity is $0.019\,\mathrm{s}^{-1} \pm 0.002\,\mathrm{s}^{-1}$. Moreover, the variation of ambient mixing ratio of $NO_2$ will change the $N_2O_5$-dissociated location in the preheating tube, which would also influence the transmission efficiency of $N_2O_5$. By assuming the $N_2O_5$ is totally dissociated in the middle of the preheating tube, we

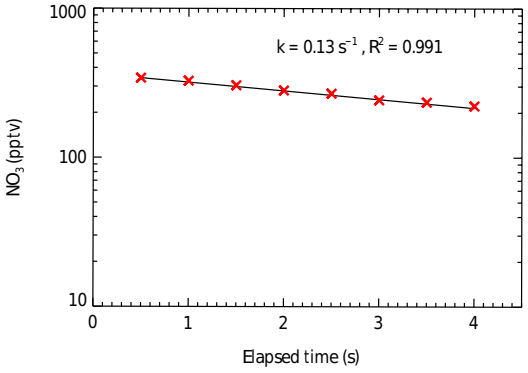


**Figure 7.** The determined concentration decay of the $NO_3$ radical in the heated detection cell caused by the wall loss. The red crosses denote the observation results, and the black line depicts the corresponding exponential fit. The net wall loss reactivity of $NO_3$ is corrected to be $0.16 \pm 0.02\,\mathrm{s}^{-1}$ with a box model simulation of the chemical reactions occurring in the detection cell.

**Table 1.** The transmission efficiency of $NO_3$ and $N_2O_5$ for the sample module setup for the developed instrument.

| Gases | Filter | Inlet tube (0.7 s) | Preheating tube (0.14 s) | Cavity (0.46 s) | Total |
|---|---|---|---|---|---|
| $NO_3$ | $72 \pm 3\,\%$[a] | $84 \pm 4\,\%$ ($k = 0.24\,s^{-1}$)[b] | 98 % ($k = 0.16\,s^{-1}$) | 93 % ($k = 0.16\,s^{-1}$) | $55 \pm 6\,\%$ |
| $N_2O_5$ | $93 \pm 3\,\%$[a] | 99 % ($k = 0.019\,s^{-1}$) | $99 \pm 1\,\%$[c] | 93 % ($k = 0.16\,s^{-1}$) | $85 \pm 3\,\%$ |

[a] Filter aging contributed an uncertainty of 3 %; [b] the uncertainty of the $NO_3$ wall loss reactivity in the cold inlet tube caused an uncertainty of 4 %; [c] the location of the $N_2O_5$ dissociation in the preheating tube had an uncertainty of 1 %.

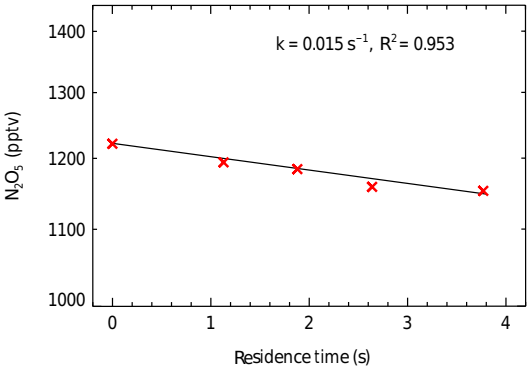


**Figure 8.** The determined concentrations of $N_2O_5$ versus the residence time of the sample gas flows in the inlet tube. The change of the residence time is achieved by changing the inlet tubes having different lengths. The red crosses denote the observation results, and the black line depicts the corresponding exponential fit. The net wall loss reactivity of $N_2O_5$ is corrected to be $0.019 \pm 0.002\,s^{-1}$ with a box model simulation of the chemical reactions occurring in the inlet tubes.

determine the transmission efficiency of $N_2O_5$ in the preheating tube to be $99 \pm 1$ %.

The total transmission efficiencies as well as the detailed contributions due to the corresponding filter and wall loss for $NO_3$ and $N_2O_5$ are summarized in Table 1 for the experimental setup during field applications. The total estimated transmission efficiency of $NO_3$ ($T_{NO_3}$) and $N_2O_5$ ($T_{N_2O_5}$) is determined to be $55 \pm 6$ and $85 \pm 3$ %, respectively. $T_{NO_3}$ is dominated by the loss on the filter and the inlet tube, and the difference of $T_{NO_3}$ between cold cavity and heated cavity is negligible, while the $T_{N_2O_5}$ is dominated by the loss on the filter and the detection cell.

### 4.3 Uncertainty and the limit of detection

As outlined above, the uncertainty of the $NO_3$ absorption is estimated to be 10 % (298 K) and 13 % (353 K), respectively; the uncertainty of the effective cavity length calculation is about 13 %, mainly due to the fast $NO_3$ wall loss; the uncertainty of the mirror reflectivity determination is about 5 %, controlled by the error of the scattering cross section of $N_2$; and the uncertainty of the $T_{NO_3}$ is about 6 %, according to the Gaussian error propagation, and the associated uncertainty is estimated to be 19 % for the ambient $NO_3$ measurement. The uncertainty of the transmission efficiency in the heated cavity is estimated at about 4 and 11 % when $N_2O_5$ or $NO_3$ dominate the concentrations of $NO_3 + N_2O_5$, respectively, according to the Gaussian error propagation, and the associated uncertainty for the ambient $NO_3 + N_2O_5$ measurement is estimated to be 19–22 %. The uncertainties of the observed mixing ratios of $NO_3$ and $NO_3 + N_2O_5$ are summarized in Table 2.

For the ambient $N_2O_5$ measurement, two parallel cavities are required with one cold cavity measures $NO_3$ and another heated cavity measured $NO_3 + N_2O_5$ like previous studies (Brown et al., 2003b; Langridge et al., 2008; Crowley et al., 2010). Here we estimated the uncertainty of $N_2O_5$ by following the expression proposed by Dubé et al. (2006).

$$\delta(N_2O_5) = \sqrt{\frac{[\delta(\mathrm{SUM})\mathrm{SUM}]^2 + [\delta(T_{NO_3})\,T_{NO_3}NO_3]^2}{[\mathrm{SUM} - T_{NO_3}NO_3]^2} + \delta\left(T_{N_2O_5}\right)^2}. \quad (3)$$

In Eq. (3), the $\delta(N_2O_5)$ represents the uncertainty of $N_2O_5$ measurements, SUM is the measured $NO_3 + N_2O_5$ in the heated cavity, $NO_3$ is the ambient mixing ratio of $NO_3$ derived by the cold cavity, $\delta(T_{NO_3})$ and $\delta(T_{N_2O_5})$ denote the uncertainty of $T_{NO_3}$ and $T_{N_2O_5}$, and $\delta(\mathrm{SUM})$ denotes the uncertainty of $NO_3 + N_2O_5$ measurement in the heated cavity. As reported by Osthoff et al. (2007) and Kennedy et al. (2011), the uncertainty of $N_2O_5$ increases with the decreasing of the ratio of $N_2O_5/NO_3$; when $N_2O_5/NO_3$ is larger than 1 in the field measurement, the uncertainty of $N_2O_5$ is in the range of 22–36 %.

The best integration time is determined through an Allan variance method (Allan, 1966; Werle et al., 1993). Figure 9a depicts the Allan variance analysis of the 12 000 zero measurement spectrums in the laboratory with 1 s integration time. According to the Allan deviation plot, increasing the integration time could improve the sensitivity of our instrument when the averaging time is smaller than 30 s. When the average time interval ranges from 30 to 100 s, the best detection capability is achieved; and when the average time interval is larger than 100 s, increasing the average time does not improve the sensitivity further and actually decreases it, which is most likely due to the drift of the light source. The limit of detection can be estimated by the standard deviation calculation from zero air measurements with the best integration time estimated above. Figure 9b and c show the histogram

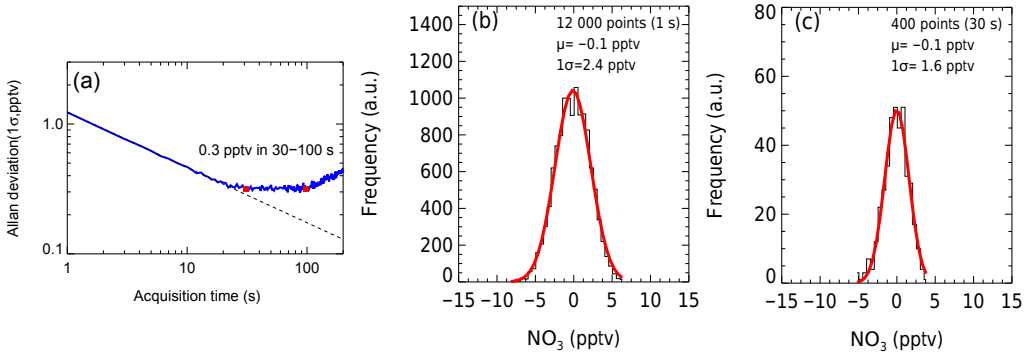


**Figure 9.** The instrument performance with different integration times. **(a)** Allan deviation plots for measurements of $NO_3$ with 1 s integration time. Panels **(b)** and **(c)** show the histogram analyses of the measurements of $NO_3$ with 1 and 30 s integration time, respectively.

**Table 2.** Details of the uncertainties of the measurement of ambient $NO_3$ and $NO_3 + N_2O_5$.

| Parameters | Uncertainty ($NO_3$) | Uncertainty ($NO_3 + N_2O_5$) |
|---|---|---|
| Cross section of $NO_3$ | 13 % | 10 % |
| Mirror reflectivity | 5 % | 5 % |
| Transmission efficiency | 6 % | 4–11 % |
| Effective cavity length | 13 % | 13 % |
| Total | 19 % | 19–22 % |

analysis of 12 000 zero measurement results for a 1 and 30 s average, respectively. The limit of detection is 2.4 pptv ($1\sigma$) for the 1 s data and improved to be 1.6 pptv ($1\sigma$) for the 30 s data. Due to the smaller cross section of $NO_3$ that was applied in the measurement of $N_2O_5$ at 353K, the LOD is estimated 2.7 pptv ($1\sigma$) with 1 s integral time. Referring to the observed mixing ratios of $NO_3$ and $N_2O_5$ in the typical regions (H. C. Wang et al., 2015), the developed instrument has the ability to measure $NO_3$ and $N_2O_5$ in the field. The LOD and uncertainty of our instrument is further compared with the existing field measurement techniques for $NO_3$ and $N_2O_5$ (Table 3). For the $NO_3$ measurement, CRDS, CEAS, and LIF are available with LOD values of 0.2-10 pptv and uncertainties lower than 25 %. For the $N_2O_5$ measurement, the three methods mentioned above and CIMS are available with LOD values of 0.5–12 pptv and uncertainties lower than 40 %. Our instrument compares well with the available field instruments for the detection of $NO_3$ and $N_2O_5$. Nevertheless, we have so far only probed the field sites with the presence of high concentrations of $NO_3 + N_2O_5$, and, therefore, the $NO_3$ measurement mode is not used in the field studies.

## 5 Performance in field campaigns

The instrument has been deployed in two comprehensive field campaigns in Beijing in 2016. The first campaign took place at the campus of the University of Chinese Academy of Sciences, and the data shown in Fig. 10b are from 27 February to 4 March, while the second campaign took place at the Peking University Changping, PKU(CP), campus and the data shown in Fig. 10c are from 23 to 29 May. As shown in Fig. 10a, both sites are located in the northern rural areas in Beijing, about 60 and 40 km from the centre of Beijing, respectively. According to our current understanding of the $NO_3$–$N_2O_5$ chemistry, rural areas lack fresh NO emissions, and the air masses transported from urban areas are well aged and featured with high $NO_2$ and $O_3$ and low NO, so that the influence of the $NO_3$–$N_2O_5$ chemistry can be maximized. We therefore expected these two sites to be ideal locations to probe the $NO_3$–$N_2O_5$ chemistry in Beijing.

During the UCAS campaign, our instrument was deployed at a roof lab, and the sample inlet was about 15 m above the ground. The measurement site was close to the mountainous area in Beijing and also was influenced by nearby traffic emissions. When the northerly wind appeared, we sampled clean air masses entrained with local traffic and residential emissions; when the southerly wind appeared, we could then capture the outflow from Beijing. In this campaign, the average night-time temperature and $NO_2$ mixing ratio is −4.3 °C and 15.5 ppbv, respectively. The calculated ratio of $N_2O_5$/ $NO_3$ based on the thermodynamic equilibrium was found to be larger than 300; therefore, the mixing ratio of $NO_3$ was ignorable compared with $N_2O_5$. Therefore, the amount of the detected $NO_3 + N_2O_5$ represented that of $N_2O_5$ for this campaign. Figure 10b shows the mixing ratio of $NO_3 + N_2O_5$ during a typical time when such air mass changes from clean to polluted conditions. High mixing ratios of $NO_3 + N_2O_5$ were observed near the ground surface at the UCAS site. During the pollution episodes, the maximum $NO_3 + N_2O_5$ reached more than 1 ppbv on the night of 2–3 March 2016. A rapid variation of $NO_3 + N_2O_5$ was also observed, which may have been due to local traffic emissions during stagnant conditions. In all these days, the observed $NO_3 + N_2O_5$ continuously accumulated during a few hours after sunset, reached its maximum before midnight,

**Table 3.** Limits of detection (LODs) and uncertainty of the existing field-deployable instruments of $NO_3$ and $N_2O_5$.

| Reference | Method | $NO_3$ | | $N_2O_5$ | |
|---|---|---|---|---|---|
| | | LOD | Uncertainty | LOD | Uncertainty |
| This work | CEAS | 2.4 pptv (1 s) | 19 % | 2.7 pptv (1 s) | 22–36 % |
| Kennedy et al. (2011) | CEAS | 1.1 pptv (1 s) | 11 % | 2.4 pptv (1 s) | 14 % |
| Bitter et al. (2005) | CEAS | 1 pptv (100 s) | | | |
| Schuster et al. (2009) | CRDS/CEAS | 2 pptv (5 s) | 14 % | 2 pptv (5 s) | 13 % |
| Nakayama et al. (2008) | CRDS | 1.5 pptv (100 s) | | | |
| Dubé et al. (2006) | CRDS | 0.2 pptv (1 s) | 25 % | 0.5pptv (1 s) | 20–40 % |
| Ayers et al. (2005) | CRDS | | | 2 pptv (25 s) | |
| D. Wang et al. (2015) | CRDS | 3.2 pptv (10 s) | 8 % | | |
| Matsumoto et al. (2005) | LIF | 10 pptv (600 s) | 17 % | 12 pptv (600 s) | 17 % |
| Slusher et al. (2004) | CIMS | | | 12 pptv (1 s) | |
| Kercher et al. (2009) | CIMS | | | 2.7 pptv (60 s) | 20 % |
| Wang et al. (2016) | CIMS | | | 4 pptv (60 s) | 20 % |

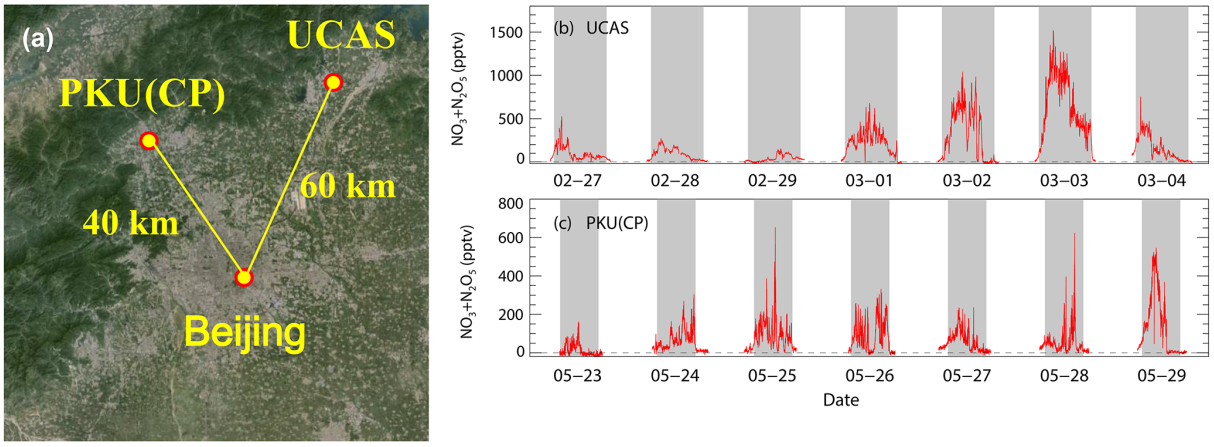


**Figure 10.** Two example time series of the observed mixing ratios of $NO_3 + N_2O_5$ measured during the UCAS winter campaign 2016 and the PKU(CP) summer campaign. The grey box indicates the time span for night-time. Panel **(a)** depicts the map of the two sites, indicating the UCAS site and the PKU(CP) site, that are about 60 and 40 km away from the centre of Beijing, respectively. Panel **(b)** shows a typical development of the observed mixing ratio of $NO_3 + N_2O_5$ from clean to polluted air masses at UCAS. Panel **(c)** shows the observed mixing ratio of $NO_3 + N_2O_5$ during a typical pollution episode at PKU(CP).

and then gradually decreased to zero before sunrise. The decrease of $NO_3 + N_2O_5$ at night in this location may be related to the typical running style of the heavy-duty vehicles (HDVs). It is known that HDVs would emit large amounts of fresh NO. The emitted NO is titrated with the $O_3$ and $NO_3$ and then reduces the accumulation of $N_2O_5$ or enhances the loss of $N_2O_5$ during the time scale of thermal dissociation (0.1–20 min from summer to winter time). Typically, more heavy-duty cars appear on the nearby street after 22:00 CST (China Standard Time, UTC + 8 h), since the ban of HDVs entering downtown Beijing is lifted after 22:00 CST. The $NO_3 + N_2O_5$ measurement results of the PKU(CP) summer campaign are presented in Fig. 10c. During the summer campaign, the instrument was set up on the fifth floor of the main building at the PKU(CP) campus. The inlet was also about 15 m above ground. The average night-time temperature and $NO_2$ mixing ratio were 10.0 °C and 17.5 ppbv, respectively. High-$O_3$ events frequently occurred in this season compared to that of winter. Together with the atmospheric processes with high-$NO_2$ conditions, the calculated ratio of $N_2O_5/NO_3$ based on the thermodynamic equilibrium was estimated to be larger than 20, and the amount of $NO_3 + N_2O_5$ also represented that of $N_2O_5$ mostly at the PKU(CP) site.

## 6 Conclusions

A new portable CEAS instrument was developed for the ambient measurement of $NO_3$ and $N_2O_5$ incorporating two unique features:

1. Novel non-adjustable mechanically aligned mirror mounts were designed and tested successfully. The new design offered a fast setup of the instrument in the field and proved to be stably operable by checking the mirror reflectivity.

2. An additional chemical titration module was tested by adding NO into the sample flow and proved to be very helpful for the ambient spectral analysis, which enhanced the fitting precision by avoiding the complicated fitting of the water vapour absorption.

The total transmission efficiencies of $NO_3$ and $N_2O_5$ were determined to be $55 \pm 6$ and $85 \pm 3$ %, respectively. The total uncertainty of the measurement of $NO_3$ and $N_2O_5$ was determined to be 19 and 22–36 %, respectively. The best limit of detection was quantified to be 2.4 pptv ($1\sigma$) and 2.7 pptv ($1\sigma$), with a 1 s integration time for $NO_3$ and $N_2O_5$, respectively. Compared to the other field instruments used worldwide, the new instrument was capable of measuring both $NO_3$ and $N_2O_5$, since only one channel was established at the moment. The instrument was deployed successfully in the $NO_3 + N_2O_5$ measurement in two comprehensive field campaigns conducted in the northern rural areas of Beijing in 2016, where high ratios of $N_2O_5/NO_3$ were present due to the presence of high $NO_2$. In these two campaigns, high mixing ratios of near-surface $NO_3 + N_2O_5$ (mostly $N_2O_5$) up to 1 ppbv were detected. The observed high $NO_3 + N_2O_5$ concentrations in the summer campaign indicated that high concentrations of $NO_3$, up to 50 pptv, could be present at night. Since significant night-time OH concentrations (up to $1 \times 10^6$ cm$^{-3}$) were also found for these environments (e.g. Lu et al., 2014; Tan et al., 2017), the contribution of $NO_3$–$N_2O_5$ and $HO_x$ chemistry toward the night-time oxidation capacity in Beijing is worthy of future exploration.

*Data availability.* The datasets used in this study are available from the corresponding author upon request (k.lu@pku.edu.cn).

*Competing interests.* The authors declare that they have no conflict of interest.

*Acknowledgements.* The work was supported by the National Natural Science Foundation of China (grants no. 41375124, 21522701, 91544225, and 41421064) and Strategic Priority Research Program of the Chinese Academy of Sciences (grant no. XDB05010500). The authors gratefully acknowledge the discussions and suggestions from Steven Brown, Kyung-Eun Min, Bin Ouyang, Ravi Varma, Hendrik Fuchs, and Zhiguo Wu. We thank the teams of the UCAS (organized by Yuanhang Zhang) and Changping campaigns (organized by Min Hu and Mattias Hallquist).

Edited by: G. Phillips
Reviewed by: two anonymous referees

## References

Aldener, M., Brown, S. S., Stark, H., Williams, E. J., Lerner, B. M., Kuster, W. C., Goldan, P. D., Quinn, P. K., Bates, T. S., Fehsenfeld, F. C., and Ravishankara, A. R.: Reactivity and loss mechanisms of $NO_3$ and $N_2O_5$ in a polluted marine environment: Results from in situ measurements during New England Air Quality Study 2002, J. Geophys. Res.-Atmos., 111, D23S73, doi:10.1029/2006jd007252, 2006.

Allan, D. W.: Statistics of Atomic Frequency Standards, Pr. Inst. Electr. Elect., 54, 221–230, 1966.

Axson, J. L., Washenfelder, R. A., Kahan, T. F., Young, C. J., Vaida, V., and Brown, S. S.: Absolute ozone absorption cross section in the Huggins Chappuis minimum (350–470 nm) at 296 K, Atmos. Chem. Phys., 11, 11581–11590, doi:10.5194/acp-11-11581-2011, 2011.

Ayers, J. D., Apodaca, R. L., Simpson, W. R., and Baer, D. S.: Off-axis cavity ring down spectroscopy: application to atmospheric nitrate radical detection, Appl. Optics, 44, 7239–7242, 2005.

Benton, A. K., Langridge, J. M., Ball, S. M., Bloss, W. J., Dall'Osto, M., Nemitz, E., Harrison, R. M., and Jones, R. L.: Night-time chemistry above London: measurements of $NO_3$ and $N_2O_5$ from the BT Tower, Atmos. Chem. Phys., 10, 9781–9795, doi:10.5194/acp-10-9781-2010, 2010.

Bitter, M., Ball, S. M., Povey, I. M., and Jones, R. L.: A broadband cavity ringdown spectrometer for in situ measurements of atmospheric trace gases, Atmos. Chem. Phys., 5, 2547–2560, doi:10.5194/acp-5-2547-2005, 2005.

Brown, S. S. and Stutz, J.: Nighttime radical observations and chemistry, Chem. Soc. Rev., 41, 6405–6447, 2012.

Brown, S. S., Stark, H., Ciciora, S. J., and Ravishankara, A. R.: In-situ measurement of atmospheric $NO_3$ and $N_2O_5$ via cavity ring-down spectroscopy, Geophys. Res. Lett., 28, 3227–3230, 2001.

Brown, S. S., Stark, H., Ciciora, S. J., McLaughlin, R. J., and Ravishankara, A. R.: Simultaneous in situ detection of atmospheric $NO_3$ and $N_2O_5$ via cavity ring-down spectroscopy, Rev. Sci. Instrum., 73, 3291–3301, 2002.

Brown, S. S., Stark, H., and Ravishankara, A. R.: Applicability of the steady state approximation to the interpretation of atmospheric observations of $NO_3$ and $N_2O_5$, J. Geophys. Res.-Atmos., 108, 4539, doi:10.1029/2003jd003407, 2003a.

Brown, S. S., Stark, H., Ryerson, T. B., Williams, E. J., Nicks, D. K., Trainer, M., Fehsenfeld, F. C., and Ravishankara, A. R.: Nitrogen oxides in the nocturnal boundary layer: Simultaneous in situ measurements of $NO_3$, $N_2O_5$, $NO_2$, NO, and $O_3$, J. Geophys. Res.-Atmos., 108, 4299, doi:10.1029/2002jd002917, 2003b.

Brown, S. S., Ryerson, T. B., Wollny, A. G., Brock, C. A., Peltier, R., Sullivan, A. P., Weber, R. J., Dubé, W. P., Trainer, M., Meagher, J. F., Fehsenfeld, F. C., and Ravishankara, A. R.: Variability in nocturnal nitrogen oxide processing and its role in regional air quality, Science, 311, 67–70, 2006.

Brown, S. S., Dubé, W. P., Tham, Y. J., Zha, Q. Z., Xue, L. K., Poon, S., Wang, Z., Blake, D. R., Tsui, W., Parrish, D. D., and Wang, T.: Nighttime chemistry at a high altitude site above Hong Kong, J. Geophys. Res.-Atmos., 121, 2457–2475, 2016.

Chang, W. L., Bhave, P. V., Brown, S. S., Riemer, N., Stutz, J., and Dabdub, D.: Heterogeneous Atmospheric Chemistry, Ambient Measurements, and Model Calculations of $N_2O_5$: A Review, Aerosol Sci. Tech., 45, 665–695, 2011.

Chen, J. and Venables, D. S.: A broadband optical cavity spectrometer for measuring weak near-ultraviolet absorption spectra of gases, Atmos. Meas. Tech., 4, 425–436, doi:10.5194/amt-4-425-2011, 2011.

Crowley, J. N., Schuster, G., Pouvesle, N., Parchatka, U., Fischer, H., Bonn, B., Bingemer, H., and Lelieveld, J.: Nocturnal nitrogen oxides at a rural mountain-site in south-western Germany, Atmos. Chem. Phys., 10, 2795–2812, doi:10.5194/acp-10-2795-2010, 2010.

Dorn, H.-P., Apodaca, R. L., Ball, S. M., Brauers, T., Brown, S. S., Crowley, J. N., Dubé, W. P., Fuchs, H., Häseler, R., Heitmann, U., Jones, R. L., Kiendler-Scharr, A., Labazan, I., Langridge, J. M., Meinen, J., Mentel, T. F., Platt, U., Pöhler, D., Rohrer, F., Ruth, A. A., Schlosser, E., Schuster, G., Shillings, A. J. L., Simpson, W. R., Thieser, J., Tillmann, R., Varma, R., Venables, D. S., and Wahner, A.: Intercomparison of $NO_3$ radical detection instruments in the atmosphere simulation chamber SAPHIR, Atmos. Meas. Tech., 6, 1111–1140, doi:10.5194/amt-6-1111-2013, 2013.

Dubé, W. P., Brown, S. S., Osthoff, H. D., Nunley, M. R., Ciciora, S. J., Paris, M. W., McLaughlin, R. J., and Ravishankara, A. R.: Aircraft instrument for simultaneous, in situ measurement of $NO_3$ and $N_2O_5$ via pulsed cavity ring-down spectroscopy, Rev. Sci. Instrum., 77, 034101, doi:10.1063/1.2176058, 2006.

Fiedler, S. E., Hese, A., and Ruth, A. A.: Incoherent broad-band cavity-enhanced absorption spectroscopy, Chem. Phys. Lett., 371, 284–294, 2003.

Fortner, E. C., Zhao, J., and Zhang, R.: Development of Ion Drift-Chemical Ionization Mass Spectrometry, Anal. Chem., 76, 5436–5440, 2004.

Fry, J. L., Kiendler-Scharr, A., Rollins, A. W., Wooldridge, P. J., Brown, S. S., Fuchs, H., Dubé, W., Mensah, A., dal Maso, M., Tillmann, R., Dorn, H.-P., Brauers, T., and Cohen, R. C.: Organic nitrate and secondary organic aerosol yield from $NO_3$ oxidation of $\beta$-pinene evaluated using a gas-phase kinetics/aerosol partitioning model, Atmos. Chem. Phys., 9, 1431–1449, doi:10.5194/acp-9-1431-2009, 2009.

Fuchs, H., Dubé, W. P., Cicioira, S. J., and Brown, S. S.: Determination of inlet transmission and conversion efficiencies for in situ measurements of the nocturnal nitrogen oxides, $NO_3$, $N_2O_5$ and $NO_2$, via pulsed cavity ring-down spectroscopy, Anal. Chem., 80, 6010–6017, 2008.

Fuchs, H., Simpson, W. R., Apodaca, R. L., Brauers, T., Cohen, R. C., Crowley, J. N., Dorn, H.-P., Dubé, W. P., Fry, J. L., Häseler, R., Kajii, Y., Kiendler-Scharr, A., Labazan, I., Matsumoto, J., Mentel, T. F., Nakashima, Y., Rohrer, F., Rollins, A. W., Schuster, G., Tillmann, R., Wahner, A., Wooldridge, P. J., and Brown, S. S.: Comparison of $N_2O_5$ mixing ratios during $NO_3$Comp 2007 in SAPHIR, Atmos. Meas. Tech., 5, 2763–2777, doi:10.5194/amt-5-2763-2012, 2012.

Gherman, T., Venables, D. S., Vaughan, S., Orphal, J., and Ruth, A. A.: Incoherent broadband cavity-enhanced absorption spectroscopy in the near-ultraviolet: Application to HONO and $NO_2$, Environ. Sci. Technol., 42, 890–895, 2008.

Kahan, T. F., Washenfelder, R. A., Vaida, V., and Brown, S. S.: Cavity-Enhanced Measurements of Hydrogen Peroxide Absorption Cross Sections from 353 to 410 nm, J. Phys. Chem. A, 116, 5941–5947, 2012.

Kennedy, O. J., Ouyang, B., Langridge, J. M., Daniels, M. J. S., Bauguitte, S., Freshwater, R., McLeod, M. W., Ironmonger, C., Sendall, J., Norris, O., Nightingale, R., Ball, S. M., and Jones, R. L.: An aircraft based three channel broadband cavity enhanced absorption spectrometer for simultaneous measurements of $NO_3$, $N_2O_5$ and $NO_2$, Atmos. Meas. Tech., 4, 1759–1776, doi:10.5194/amt-4-1759-2011, 2011.

Kercher, J. P., Riedel, T. P., and Thornton, J. A.: Chlorine activation by $N_2O_5$: simultaneous, in situ detection of $ClNO_2$ and $N_2O_5$ by chemical ionization mass spectrometry, Atmos. Meas. Tech., 2, 193–204, doi:10.5194/amt-2-193-2009, 2009.

Langridge, J. M., Laurila, T., Watt, R. S., Jones, R. L., Kaminski, C. F., and Hult, J.: Cavity enhanced absorption spectroscopy of multiple trace gas species using a supercontinuum radiation source, Opt. Express, 16, 10178–10188, 2008.

Lu, K. D., Rohrer, F., Holland, F., Fuchs, H., Brauers, T., Oebel, A., Dlugi, R., Hu, M., Li, X., Lou, S. R., Shao, M., Zhu, T., Wahner, A., Zhang, Y. H., and Hofzumahaus, A.: Nighttime observation and chemistry of $HO_x$ in the Pearl River Delta and Beijing in summer 2006, Atmos. Chem. Phys., 14, 4979–4999, doi:10.5194/acp-14-4979-2014, 2014.

Matsumoto, J., Kosugi, N., Imai, H., and Kajii, Y.: Development of a measurement system for nitrate radical and dinitrogen pentoxide using a thermal conversion/laser-induced fluorescence technique, Rev. Sci. Instrum., 76, 064101, doi:10.1063/1.1927098, 2005.

Min, K.-E., Washenfelder, R. A., Dubé, W. P., Langford, A. O., Edwards, P. M., Zarzana, K. J., Stutz, J., Lu, K., Rohrer, F., Zhang, Y., and Brown, S. S.: A broadband cavity enhanced absorption spectrometer for aircraft measurements of glyoxal, methylglyoxal, nitrous acid, nitrogen dioxide, and water vapor, Atmos. Meas. Tech., 9, 423–440, doi:10.5194/amt-9-423-2016, 2016.

Nakayama, T., Ide, T., Taketani, F., Kawai, M., Takahashi, K., and Matsumi, Y.: Nighttime measurements of ambient $N_2O_5$, $NO_2$, NO and $O_3$ in a sub-urban area, Toyokawa, Japan, Atmos. Environ., 42, 1995–2006, 2008.

Orphal, J., Fellows, C. E., and Flaud, P. M.: The visible absorption spectrum of $NO_3$ measured by high-resolution Fourier transform spectroscopy, J. Geophys. Res.-Atmos., 108, 4077, doi:10.1029/2002jd002489, 2003.

Osthoff, H. D., Pilling, M. J., Ravishankara, A. R., and Brown, S. S.: Temperature dependence of the $NO_3$ absorption cross-section above 298 K and determination of the equilibrium constant for $NO_3 + NO_2 \leftrightarrow N_2O_5$ at atmospherically relevant conditions, Phys. Chem. Chem. Phys., 9, 5785–5793, 2007.

Osthoff, H. D., Roberts, J. M., Ravishankara, A. R., Williams, E. J., Lerner, B. M., Sommariva, R., Bates, T. S., Coffman, D., Quinn, P. K., Dibb, J. E., Stark, H., Burkholder, J. B., Talukdar, R. K., Meagher, J., Fehsenfeld, F. C., and Brown, S. S.: High levels of nitryl chloride in the polluted subtropical marine boundary layer, Nat. Geosci., 1, 324–328, 2008.

Phillips, G. J., Tang, M. J., Thieser, J., Brickwedde, B., Schuster, G., Bohn, B., Lelieveld, J., and Crowley, J. N.: Significant concentrations of nitryl chloride observed in rural continental Europe associated with the influence of sea salt chloride and anthropogenic emissions, Geophys. Res. Lett., 39, L10811, doi:10.1029/2012GL051912, 2012.

Ravishankara, A. R. and Mauldin, R. L.: Temperature-Dependence of the $NO_3$ Cross-Section in the 662-Nm Region, J. Geophys. Res.-Atmos., 91, 8709–8712, 1986.

Richter, A., Burrows, J. P., Nuss, H., Granier, C., and Niemeier, U.: Increase in tropospheric nitrogen dioxide over China observed from space, Nature, 437, 129–132, 2005.

Riemer, N., Vogel, H., Vogel, B., Schell, B., Ackermann, I., Kessler, C., and Hass, H.: Impact of the heterogeneous hydrolysis of $N_2O_5$ on chemistry and nitrate aerosol formation in the lower troposphere under photosmog conditions, J. Geophys. Res.-Atmos., 108, 4144, doi:10.1029/2002jd002436, 2003.

Sander, S. P.: Temperature-Dependence of the No3 Absorption-Spectrum, J. Phys. Chem.-US, 90, 4135–4142, 1986.

Schuster, G., Labazan, I., and Crowley, J. N.: A cavity ring down/cavity enhanced absorption device for measurement of ambient $NO_3$ and $N_2O_5$, Atmos. Meas. Tech., 2, 1–13, doi:10.5194/amt-2-1-2009, 2009.

Shardanand, S. and Rao, A. D. P.: Absolute Rayleigh scattering cross sections of gases and freons of stratospheric interest in the visible and ultraviolet regions, NASA Technical Note, Alabama, USA, 1977.

Simpson, W. R.: Continuous wave cavity ring-down spectroscopy applied to in situ detection of dinitrogen pentoxide ($N_2O_5$), Rev. Sci. Instrum., 74, 3442–3452, 2003.

Slusher, D. L., Huey, L. G., Tanner, D. J., Flocke, F. M., and Roberts, J. M.: A thermal dissociation-chemical ionization mass spectrometry (TD-CIMS) technique for the simultaneous measurement of peroxyacyl nitrates and dinitrogen pentoxide, J. Geophys. Res.-Atmos., 109, D19315, doi:10.1029/2004jd004670, 2004.

Sneep, M. and Ubachs, W.: Direct measurement of the Rayleigh scattering cross section in various gases, J. Quant. Spectrosc. Ra., 92, 293–310, 2005.

Sobanski, N., Tang, M. J., Thieser, J., Schuster, G., Pöhler, D., Fischer, H., Song, W., Sauvage, C., Williams, J., Fachinger, J., Berkes, F., Hoor, P., Platt, U., Lelieveld, J., and Crowley, J. N.: Chemical and meteorological influences on the lifetime of $NO_3$ at a semi-rural mountain site during PARADE, Atmos. Chem. Phys., 16, 4867–4883, doi:10.5194/acp-16-4867-2016, 2016.

Tan, Z., Fuchs, H., Lu, K., Hofzumahaus, A., Bohn, B., Broch, S., Dong, H., Gomm, S., Häseler, R., He, L., Holland, F., Li, X., Liu, Y., Lu, S., Rohrer, F., Shao, M., Wang, B., Wang, M., Wu, Y., Zeng, L., Zhang, Y., Wahner, A., and Zhang, Y.: Radical chemistry at a rural site (Wangdu) in the North China Plain: observation and model calculations of OH, $HO_2$ and $RO_2$ radicals, Atmos. Chem. Phys., 17, 663–690, doi:10.5194/acp-17-663-2017, 2017.

Thalman, R. and Volkamer, R.: Inherent calibration of a blue LED-CE-DOAS instrument to measure iodine oxide, glyoxal, methyl glyoxal, nitrogen dioxide, water vapour and aerosol extinction in open cavity mode, Atmos. Meas. Tech., 3, 1797–1814, doi:10.5194/amt-3-1797-2010, 2010.

Tham, Y. J., Wang, Z., Li, Q., Yun, H., Wang, W., Wang, X., Xue, L., Lu, K., Ma, N., Bohn, B., Li, X., Kecorius, S., Größ, J., Shao, M., Wiedensohler, A., Zhang, Y., and Wang, T.: Significant concentrations of nitryl chloride sustained in the morning: investigations of the causes and impacts on ozone production in a polluted region of northern China, Atmos. Chem. Phys., 16, 14959–14977, doi:10.5194/acp-16-14959-2016, 2016.

Thornton, J. A., Kercher, J. P., Riedel, T. P., Wagner, N. L., Cozic, J., Holloway, J. S., Dubé, W. P., Wolfe, G. M., Quinn, P. K., Middlebrook, A. M., Alexander, B., and Brown, S. S.: A large atomic chlorine source inferred from mid-continental reactive nitrogen chemistry, Nature, 464, 271–274, 2010.

Varma, R. M., Venables, D. S., Ruth, A. A., Heitmann, U., Schlosser, E., and Dixneuf, S.: Long optical cavities for open-path monitoring of atmospheric trace gases and aerosol extinction, Appl. Optics, 48, B159–B171, 2009.

Venables, D. S., Gherman, T., Orphal, J., Wenger, J. C., and Ruth, A. A.: High sensitivity in situ monitoring of $NO_3$ in an atmospheric simulation chamber using incoherent broadband cavity-enhanced absorption spectroscopy, Environ. Sci. Technol., 40, 6758–6763, 2006.

Voigt, S., Orphal, J., and Burrows, J. P.: The temperature and pressure dependence of the absorption cross-sections of $NO_2$ in the 250–800 nm region measured by Fourier-transform spectroscopy, J. Photoch. Photobio. A, 149, 1–7, 2002.

Wang, D., Hu, R. Z., Xie, P. H., Liu, J. G., Liu, W. Q., Qin, M., Ling, L. Y., Zeng, Y., Chen, H., Xing, X. B., Zhu, G. L., Wu, J., Duan, J., Lu, X., and Shen, L. L.: Diode laser cavity ring-down spectroscopy for in situ measurement of $NO_3$ radical in ambient air, J. Quant. Spectrosc. Ra., 166, 23–29, 2015.

Wang, H. C., Chen, J., and Lu, K. D.: Measurement of $NO_3$ and $N_2O_5$ in the Troposphere, Prog. Chem., 27, 963–976, 2015.

Wang, S. S., Shi, C. Z., Zhou, B., Zhao, H., Wang, Z. R., Yang, S. N., and Chen, L. M.: Observation of $NO_3$ radicals over Shanghai, China, Atmos. Environ., 70, 401–409, 2013.

Wang, T., Tham, Y. J., Xue, L. K., Li, Q. Y., Zha, Q. Z., Wang, Z., Poon, S. C. N., Dubé, W. P., Blake, D. R., Louie, P. K. K., Luk, C. W. Y., Tsui, W., and Brown, S. S.: Observations of nitryl chloride and modeling its source and effect on ozone in the planetary boundary layer of southern China, J. Geophys. Res.-Atmos., 121, 2476–2489, 2016.

Wang, X., Wang, T., Yan, C., Tham, Y. J., Xue, L., Xu, Z., and Zha, Q.: Large daytime signals of $N_2O_5$ and $NO_3$ inferred at 62 amu in a TD-CIMS: chemical interference or a real atmospheric phenomenon?, Atmos. Meas. Tech., 7, 1–12, doi:10.5194/amt-7-1-2014, 2014.

Wangberg, I., Etzkorn, T., Barnes, I., Platt, U., and Becker, K. H.: Absolute determination of the temperature behavior of the $NO_2 + NO_3 + (M) \leftrightarrow N_2O_5 + (M)$ equilibrium, J. Phys. Chem. A, 101, 9694–9698, 1997.

Washenfelder, R. A., Langford, A. O., Fuchs, H., and Brown, S. S.: Measurement of glyoxal using an incoherent broadband cavity enhanced absorption spectrometer, Atmos. Chem. Phys., 8, 7779–7793, doi:10.5194/acp-8-7779-2008, 2008.

Washenfelder, R. A., Flores, J. M., Brock, C. A., Brown, S. S., and Rudich, Y.: Broadband measurements of aerosol extinction in the ultraviolet spectral region, Atmos. Meas. Tech., 6, 861–877, doi:10.5194/amt-6-861-2013, 2013.

Washenfelder, R. A., Attwood, A. R., Flores, J. M., Zarzana, K. J., Rudich, Y., and Brown, S. S.: Broadband cavity-enhanced absorption spectroscopy in the ultraviolet spectral region for measurements of nitrogen dioxide and formaldehyde, Atmos. Meas. Tech., 9, 41–52, doi:10.5194/amt-9-41-2016, 2016.

Wayne, R. P., Barnes, I., Biggs, P., Burrows, J. P., Canosa-Mas, C. E., Hjorth, J., Le Bras, G., Moortgat, G. K., Perner, D., Poulet, G., Restelli, G., and Sidebottom, H.: The nitrate radical: Physics, chemistry, and the atmosphere, Atmos. Environ., 25A, 1–206, 1991.

Werle, P., Mucke, R., and Slemr, F.: The Limits of Signal Averaging in Atmospheric Trace-Gas Monitoring by Tunable Diode-Laser Absorption-Spectroscopy (Tdlas), Appl. Phys. B-Photo., 57, 131–139, 1993.

Yokelson, R. J., Burkholder, J. B., Fox, R. W., Talukdar, R. K., and Ravishankara, A. R.: Temperature-Dependence of the $NO_3$ Absorption-Spectrum, J. Phys. Chem.-US, 98, 13144–13150, 1994.